KSME

Springer

Journal of Mechanical Science and Technology 36 (12) 2022

Original Article
DOI 10.1007/s12206-022-1104-8

Keywords:
· Motion stage
· Friction
· Eccentric drive
· Asymmetric flexure hinge
· Uniformity

Correspondence to:
Zhijun Yang
yangzj@gdut.edu.cn

Citation:
Su, L., Huang, G., Huang, R., Yang, Z. (2022). Design of a compact long-stroke high-precision rigid-flexible coupling motion stage driven by linear motor. Journal of Mechanical Science and Technology 36 (12) (2022) 5859~5870. http://doi.org/10.1007/s12206-022-1104-8

Received March 28th, 2022
Revised August 24th, 2022
Accepted August 24th, 2022

† Recommended by Editor
No-cheol Park

Design of a compact long-stroke high-precision rigid-flexible coupling motion stage driven by linear motor

Liyun Su[1], Guanxin Huang[1], Ruirui Huang[1] and Zhijun Yang[1,2]

[1]State Key Laboratory for Precision Electronics Manufacturing Technology and Equipment, School of Mechanical Engineering, Guangdong University of Technology, Guangzhou CO 510006, China, [2]Foshan Huadao Ultra Precision Co., Ltd, Guangzhou 51006, China

Abstract This paper proposes a long-stroke rigid-flexible coupling motion stage (RFCMS) that employs flexure hinges to compensate the friction dead zone through elastic deformation. Specifically, based on the need for a motion stage with a compact structure, this paper proposes a new rigid-flexible coupling structure (RFCS) design with a horizontally installed linear motor and asymmetric flexure hinges. Further, end leaf springs are introduced to enhance the stiffness in the non-motion direction. In addition, the nonlinear interior-point optimization method is used to obtain the optimal structural parameters of the flexure hinges for higher deformation uniformity. To verify the effectiveness of the proposed design, a motion stage benchmarked with Aerotech's PRO190LM (stroke, 500 mm) is developed, which realizes bidirectional repeatability (BR) of ±0.25 μm. The BR is improved by 37.5 %. Moreover, the deformation uniformity of the stage is ±3.7 %, which proves that the proposed RFCMS can achieve high deformation uniformity and high precision.

1. Introduction

In recent years, integrated circuit (IC) manufacturing [1], optical positioning [2, 3], microscopic detection [4], and various fields have an increasing demand for high-precision positioning stages [5]. In addition, those fields require high-speed, high-acceleration, and a longer stroke range to increase the number of potential applications, such as manufacturing and precision measurement [6].

The compliant mechanisms (flexure hinges) can achieve micro/nano-precise operation [7] due to non-friction and free of backlash. Similarly, micro displacement amplification mechanisms are gaining importance in microelectromechanical system (MEMS) applications where motion precision, reliability, and compactness are needed [8]. However, the measurement and positioning range of these mechanisms is limited [9], which limits the applications for large-area operation in specific parts (solar cells, silicon chips, etc.) [10].

With the increase of positioning range from micrometer level to millimeter level, piezoelectric stack actuators (PSAs) have attracted extensive attention in precision positioning stages owing to their small volume, fast response, and low cost [9]. The combination of PSA and compliant mechanism is widely used in the mechanical structure design of the high-resolution positioning stage to amplify the finite output displacement of PSAs [11-14]. Similarly, the combination of the voice coil motor (VCM) and the compliant mechanism is also commonly used in the positioning system of the high-speed precision motion stage [15-17]. However, the amplified compliant mechanisms, no matter driven by PSA or VCM, are usually difficult to achieve long-stroke [18, 19], which can not meet the demand of long-stroke motion stage of tens of millimeters or even hundreds of millimeters.

In order to achieve both long-stroke and high precision positioning, the concept of macro-micro composite is widely used in various positioning stages [20, 21]. In previous works, Zhang et al. [22] proposed a macro-positioning stage driven by VCM and a micro-positioning stage

driven by piezoelectric ceramics. The repeat positioning accuracy is 0.2 μm in the 50 mm stroke. In 2018, Zhang [23] adopted a rapid dynamic positioning (RDP) method, reducing the setting time by 34.9 % compared with the available micro-positioning methods, enabling the stage to realize the positioning accuracy of 0.018 μm at the stroke of 40 mm. The long-stroke macro-micro motion stage developed by Shinno et al. [24] uses servo motor and ball screw as macro drive and VCM and aerostatic guideways as micro drive, which can realize positioning with a 0.3 nm resolution in a 150 mm range and enable speed and acceleration to achieve 100 mm/s and 500 mm/s^2 respectively. In the above research, millimeter level stroke and high-precision positioning can be realized, but there are some common problems: macro and micro-positioning stages need two sets of the driving systems and switching control, resulting in low efficiency. There is also a need for high-resolution measuring instruments to achieve nano-positioning, which means high cost.

Dong et al. studied a vibration assisted nanopositioning (VAN) stage [25] which is driven by permanent magnet synchronous linear motor (PMSLM). Two compliant mechanisms connect the mechanical bearings and the working stage. Their dithering force is provided by two PSAs. The stage can achieve stroke of 50 mm and a position error of 100 nm. The problem with the stage is that system is more complex due to the addition of sensors and actuators, and there are assembly errors in this stage. At present, the mechanical-bearing-guided motion stage (MBGMS) is still the mainstream of high-speed and high-precision operation due to its high rigidity and low cost. For the MBGMS, it is necessary to consider the factors that influence the accuracy of the motion stage, including nonlinear pre-motion friction [26] and the elastic deformation of the working stage, as shown in Fig. 1(a).

According to the above research, challenges in the current high-precision motion stages are the synchronous improvement of stroke and precision [10], which belong to contradictory requirements. As shown in Fig. 2, some classifications of motion stages are listed. Compliant mechanism and amplification mechanisms can achieve ultra-high precision positioning, but they have a short stroke. The macro-micro composite mode support long stroke in a relatively high precision. However, they are typically limited in control efficiency and high cost due to the complex system with dual-drive. Although the traditional MGBMS is charactered by large-stroke and high-speed, it is difficult to achieve nano-level positioning precision due to the mechanical bearing friction.

This paper proposes a rigid-flexible coupling motion stage (RFCMS) which combines the flexure hinges with the traditional MGBMS, and it is driven by PMSLM. PMSLM and mechanical bearings are used to realize long-stroke and high-speed motion. The design of rigid-flexible coupling structure (RFCS) can transform the friction into the measurable elastic deformation of flexure hinges to achieve high-precision positioning, as shown in Fig. 1(b). In order to obtain a compact structure, the PMSLM in the RFCS is installed horizontally. For

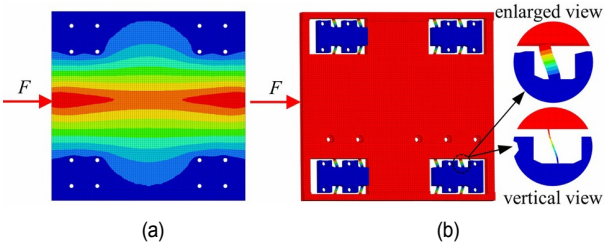

Fig. 1. Displacement contour of Traditional MBGMS and RFCS: (a) the traditional MBGMS has elastic deformation; (b) displacement contour of RFCS, the enlarged view shows the elastic deformation of the flexure hinge.

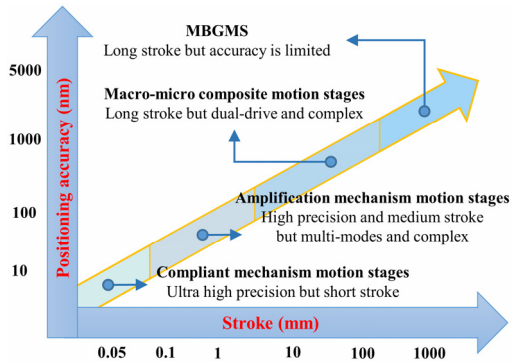

Fig. 2. Classification of motion stages.

comparability, this is the motion stage benchmarked with the PRO190LM (stroke, 500 mm) motion stage of Aerotech company, a company in the United States, whose linear motion stage module is a typical product in pursuing ultra-high precision. The structure and performance indexes of PRO190LM (stroke, 500 mm) are shown in Ref. [27].

The contributions of this research are three-folds: 1) combining flexure hinge with MGBMS, an RFCMS based on eccentric drive of PMSLM and asymmetric flexure hinge is designed, which can simultaneously realize long-stroke and high-precision; 2) an optimization design method is proposed to improve the deformation uniformity of the motion stage under eccentric force; 3) compared with the PRO190LM with the same stroke, the precision of RFCMS is significantly improved and the required resolution is lower, which means lower cost.

The rest of this paper is organized as follows. Sec. 2 introduces the structural design and working principle of RFCS. Sec. 3 introduces the optimal design method of RFCS under eccentric drive, and the feasibility of the proposed method is verified using finite element analysis (FEA). In Sec. 4, a prototype is fabricated, and the bidirectional repeatability (BR) and the deformation uniformity of the stage are verified by experiments. Finally, we summarize this paper in Sec. 5.

2. Structural design and working principle of RFCS

2.1 Structure design of RFCS

As depicted in Fig. 3(a), the RFCS based on horizontally in-

stalled PMSLM is integrated, including three parts: rigid frame, working stage and flexure hinges. The rigid frames and working stage are connected through the left flexure hinges (LFHs) and the right flexure hinges (RFHs), and the rigid frames are connected with the mechanical bearings. The PMSLM is installed under the working stage to motivate it directly, leading to the elastic deformation of the flexure hinges, and passing the driven force onto the rigid frames to move on the mechanical bearings. As depicted in Fig. 3(b), some important dimensions of RFCS are pointed out.

In general, flexure hinges are symmetrically arranged on the stage, and the driving force is also applied symmetrically [28], [29]. When using a VCM/PSA drive, as shown in Fig. 4(a), the driving force acts on the axis of symmetry along the motion direction (X-axis) of the stage; hence, only flexure hinges symmetrically arranged on both sides of the working stage are required. The stage generates nearly no displacement in the non-motion direction [30]. However, the motion stage has a short stroke in this driving mode. When a vertically installed motor is used for driving, as shown in Fig. 4(b), the driving force is applied directly under the working stage; such force is categorized as an offset driving force. This driving mode will lead to an additional bending moment in the non-motion direction (Y-axis) and a small pitch motion of the stage. When the flexure hinges are arranged symmetrically, the pitch of the working stage increases. Moreover, this mode leads to a high mass center of the stage. To meet the requirements of a low mass center and a compact structure of the motion stage, the motor is usually installed horizontally. However, this driving mode causes the stage to be affected by an eccentric driving force, which leads to additional bending moments in the non-motion directions (i.e., Y and Z), as shown in Fig. 4(c). Similarly, symmetrically arranged flexure hinges may also increase these bending moments. Therefore, space flexure hinges (SFHs) [31] are required to improve the payload stiffness and reduce the pitch motion.

In order to explore the influence of eccentric drive on the motion stage with symmetrically arranged flexure hinges, the following simulations are carried out.

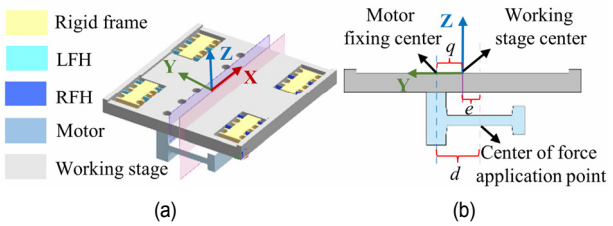

Fig. 3. Structure of RFCS: (a) RFCS; (b) important dimensions of RFCS: the distance from the working stage center to the motor fixing center is *q*, the distance from the motor fixing center to the center of force application point is *d*, and the eccentricity is *e*.

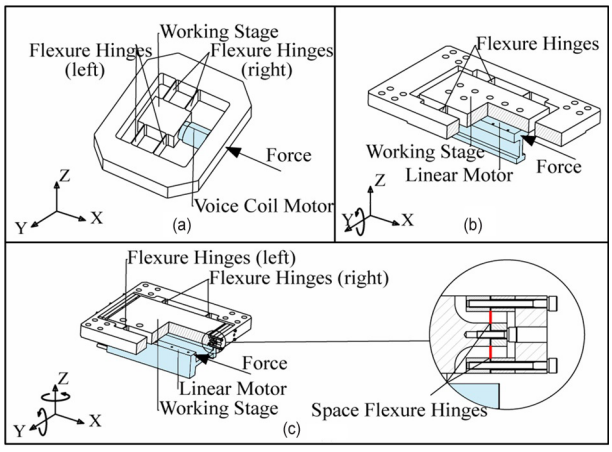

Fig. 4. Arrangement form of motor: (a) motor (e.g., VCM) is installed along the axis of symmetry in the motion direction; (b) motor (e.g., PMSLM) is vertical installation under the working stage; (c) motor (e.g., PMSLM) is horizontal installation under the stage.

2.1.1 Influence on the motion direction of the stage

Build a multi-body dynamics model of the RFCS using ADAMS, as shown in Fig. 5. Set the eccentricity *e* of the driving force to 17 mm, arrange LFHs and RFHs symmetrically in the motion direction to ensure the same stiffness of the flexure hinge, assume that the motor is rigidly connected with the working stage, and 10 N driving force is set at the center of force application point. According to the simulation result shown in Fig. 6. The displacement of RFHs is 1.64 times that of LFHs, and the value will increase with the increase of driving force. It means that the displacement in the motion direction is

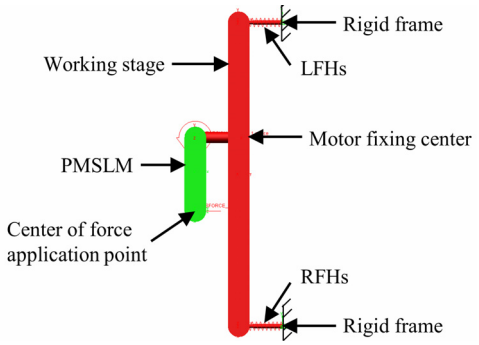

Fig. 5. RFCS model in ADAMS.

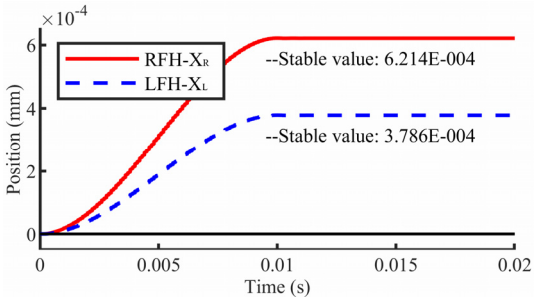

Fig. 6. Displacement curves of LFHs and RFHs.

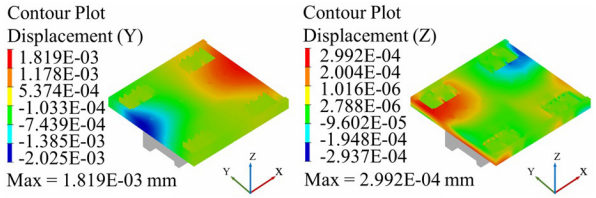

(a) (b)

Fig. 7. Stage deformation contour: (a) in Y-axis; (b) in Z-axis.

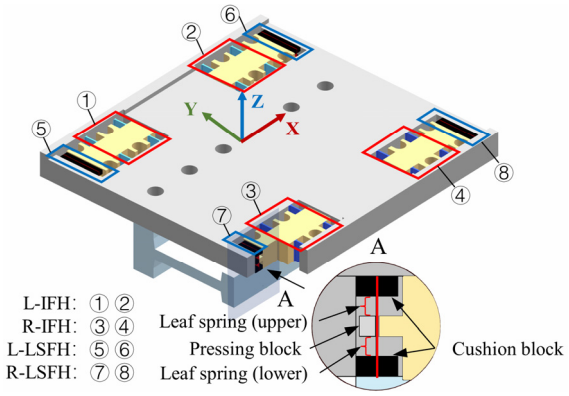

Fig. 8. RFCS with LSFHs.

extremely nonuniform, which will directly affect the positioning precision of the stage.

2.1.2 Influence on the non-motion directions of the stage

Furthermore, since the motion stage belongs to point-to-point (PTP) positioning system, the driving force in the positioning phase must be less than the continuous force of the motor. A motor with a continuous force of 166 N is applied to the RFCS with flexure hinges which are arranged symmetrically for static simulation (HyperWorks: hexahedral mesh). Among them, the driving force is applied to the PMSLM, and rigid frames are subject to fixed constraints. It can be seen that the working stage still has deformation in the non-motion directions in Fig. 7: the deformation of the Y-axis is micrometer level (a), and the deformation of the Z-axis is sub-micrometer (b), which also has a significant impact on the precision of the stage.

According to the above analysis, asymmetric flexure hinges need to be arranged to ensure the deformation uniformity of the working stage and reduce the deformation in the non-motion directions. Thus, this paper innovatively uses the high-strength leaf spring (material: 65 Mn) as the SFHs and assembles it on the integrated RFCS to enhance the stiffness in the non-motion direction. As shown in Fig. 8, the leaf spring (red) are clamped with cushion blocks and connected with the working stage, and the middle is clamped with the pressing block and connected with the rigid frame. In this way, leaf spring flexure hinges (LSFHs) are divided into the upper and lower working areas. For convenient of description, IFHs are divided into IFHs on the left (L-IFHs) and IFHs on the right (R-IFHs), and LSFHs are divided into LSFHs on the left (L-LSFHs) and LSFHs on the right (R-LSFHs). The structure of IFH and LSFH are shown in Fig. 9. Table 1 shows the material properties of RFCS.

Table 1. Material properties of RFCS.

Type	RFCS	LSFH
Material	Aluminum alloy 7075-T6	65 Mn
Density (kg/m^3)	2810	7820
Young's modulus (MPa)	72000	211000
Poisson's ratio	0.33	0.288

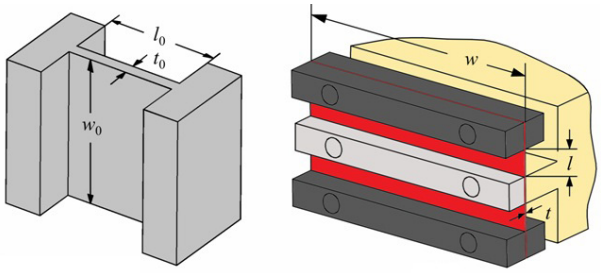

(a) (b)

Fig. 9. Structure of flexure hinge: (a) IFH; (b) LSFH.

2.2 Working principle of RFCS

The working principle of RFCS is that the motion law of the motion stage in the process of dynamic and static friction switching can be transformed from Newton's law to Hooke's law by introducing flexure hinge, and the uncertain factors caused by the nonlinear friction of the mechanical bearing can be effectively transformed into the elastic deformation through the flexure hinges. As shown in Fig. 10, the RFCS can be simplified to a mass-spring-damper model.

Where x_0 is the displacement of the working stage, and x_i (i = 1, 2, 3, 4) represents the displacements of rigid frames. m_0 is the mass of the working stage, and m_i (i = 1, 2, 3, 4) represents the mass of the rigid frame. c_i and k_i (i = 1, 2, 3, 4) are damping coefficients and stiffnesses of the working stage connecting with rigid frames, respectively. f_0 is the driving force of the motor. $f_{\mu i}$ represents the friction forces of the mechanical bearings.

The f_0 is applied to the working stage. Before the f_0 is less than the maximum static friction, the rigid frames do not produce displacement, and the flexure hinges produce elastic deformation under the drive of the working stage to compensate the positioning error, so as to realize precise positioning. When the f_0 is greater than the maximum static friction, the working stage drives the flexure hinges to produce elastic deformation, and the flexure hinges drive the rigid frames to move on the mechanical bearing to realize the long stroke motion of the stage. Moreover, when it reaches near the positioning position, the f_0 decreases, and the final positioning error continues to be compensated by the elastic deformation of the flexure

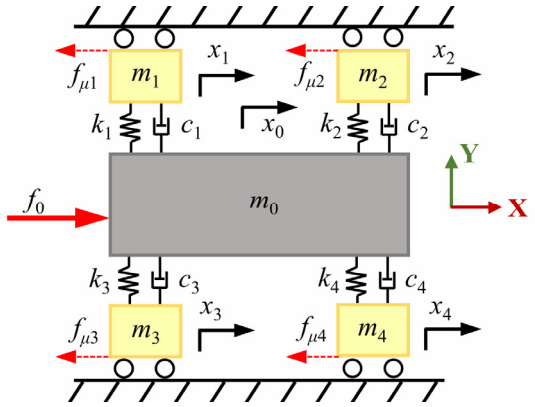

Fig. 10. The dynamic model of RFCS.

hinges.

3. Optimation design and simulation verification

Through the above design, this paper studies the RFCS under eccentric drive. A structural optimal method of flexure hinge is proposed to improve the deformation uniformity on X-axis and reduce the deformation of working stage in Y-axis and Z-axis. For the convenience of analysis, the following hypotheses are established: 1) the material is homogeneous isotropic; 2) the working stage is simplified as a rigid beam element.

3.1 Design variable

The thickness of flexure hinge has the greatest influence on its stiffness, so this paper takes the thickness of flexure hinge as the design variable. Since IFHs are only used for guiding, and to ensure the assembly of LSFHs without error, both of thickness is t_0. In order to meet the deformation uniformity in the motion direction, LSFHs adopt asymmetric arrangement: the thickness of L-LSFHs is t_1, the thickness of R-LSFHs is t_2. Therefore, three parameters t_0, t_1, t_2 need to be optimized.

3.2 Constraint function

As shown in Fig. 11, F_x is a transverse force, F_Y is an axial force, M_Z is a moment and the corresponding deflections are denoted by ΔX, ΔY, and θ_Z. According to the beam model of flexure hinge, the load-displacement relations at the free end of the beam can be established [29], as follows Eq. (1):

$$\begin{bmatrix} \frac{F_X l^2}{EI_Z} \\ \frac{M_Z l}{EI_Z} \end{bmatrix} = \begin{bmatrix} 12 & -6 \\ -6 & 4 \end{bmatrix} \begin{bmatrix} \frac{\Delta X}{l} \\ \theta_Z \end{bmatrix}, \text{ where } I_Z = \frac{wt^3}{12} \tag{1}$$

where I_Z is the second moment of area about the Z-axis, E is the Young's modulus of the material, and the length, the width,

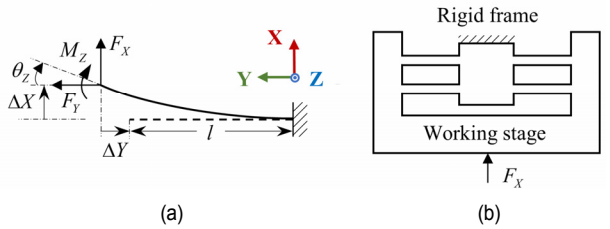

Fig. 11. (a) Beam model of flexure hinge; (b) guiding mechanism with flexure hinges.

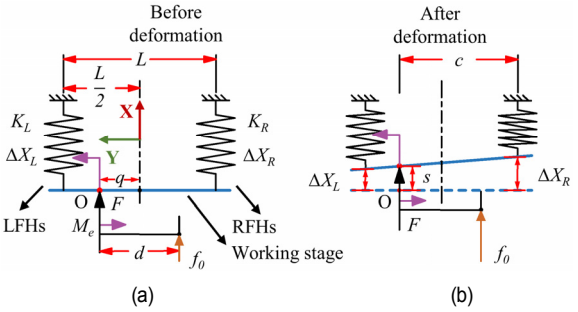

Fig. 12. RFCS simplified model.

and the thickness of a flexure hinge are denoted as l, w, and t.

Both the axial deflection and rotation of the flexure hinges in the guiding mechanism are zero. The stiffness of flexure hinge is obtained by substituting $\theta_Z = 0$ into Eq. (1):

$$\frac{F_X}{\Delta X} = \frac{12EI_Z}{l^3} = \frac{Ewt^3}{l^3}. \tag{2}$$

3.2.1 No deflection constraint

The static deformation of LFHs and RFHs should be equal.

Comparing the stiffness ratio of LFHs and RFHs between the design objective and theoretical objective which is based on the principle of minimum potential energy, they should be equal. The theoretical objective is determined as follows.

A simple model is established for the RFCS driven by eccentric force, as shown in Fig. 12. The total stiffness of the RFHs and LFHs are K_R and K_L, respectively. The corresponding total displacement under driving force f_0 is ΔX_R and ΔX_L, respectively. Point O is the motor fixing center. The model is analyzed according to the principle of minimum potential energy.

The strain energy of the system is as follows Eq. (3):

$$E = \frac{1}{2}K_R\Delta X_R^2 + \frac{1}{2}K_L\Delta X_L^2. \tag{3}$$

The total potential of the loads is as follows Eq. (4):

$$H = Fs + M_e\frac{(\Delta X_R - \Delta X_L)}{L} \tag{4}$$

where s is the displacement of point O after applied force: $s = (L-c)(\Delta X_R - \Delta X_L)/L + \Delta X_L$, and L is the length of the working

stage on Y-axis, F is the force transferred from the driving force f_0 to point O, and M_e is the moment at point O. $F = f_0$, $M_e = f_0 d$.

From the principle of minimum potential energy, the total potential energy of the system is

$$P = E - H = \frac{1}{2}K_R \triangle X_R^2 + \frac{1}{2}K_L \triangle X_L^2 - F\left[\frac{(L-c)(\triangle X_R - \triangle X_L)}{L} + \triangle X_L\right] + Fd\frac{(\triangle X_R - \triangle X_L)}{L}. \quad (5)$$

Find the derivatives of ΔX_R and ΔX_L respectively for P and make them equal to 0, then:

$$\frac{\partial P}{\partial \triangle X_R} = K_R \triangle X_R - F + \frac{Fc}{L} - \frac{Fd}{L} = 0, \quad (6)$$

$$\frac{\partial P}{\partial \triangle X_L} = K_L \triangle X_L - \frac{Fc}{L} + \frac{Fd}{L} = 0. \quad (7)$$

Therefore, the deformations are

$$\triangle X_R = \left(F - \frac{Fc}{L} + \frac{Fd}{L}\right)/K_R, \quad (8)$$

$$\triangle X_L = \left(\frac{Fc}{L} - \frac{Fd}{L}\right)/K_L. \quad (9)$$

In order to make the displacement of RFCS in the motion direction is uniform under eccentric driving, let $\Delta X_R = \Delta X_L$:

$$\left(F - \frac{Fc}{L} + \frac{Fd}{L}\right)/K_R = \left(\frac{Fc}{L} - \frac{Fd}{L}\right)/K_L. \quad (10)$$

The stiffness ratio β of the RFHs and LFHs obtained by the principle of minimum potential energy is defined as the theoretical objective, and its calculation is as follows:

$$\beta = K_L / K_R = \left[\frac{1}{L}(c-d)\right]/\left(1 - \frac{c}{L} + \frac{d}{L}\right) \quad (11)$$

where d = 34.25 mm, L = 140 mm, and c = 87.25 mm.

To verify the accuracy of the ratio, a multi-body dynamics simulation verification is carried out in ADAMS (the model is shown in Fig. 5): set K_R = 10000 N/mm, in proportion, K_L = 6092 N/mm. The rigid connection and flexible connection between the motor and the working stage are verified respectively. The displacement curves of LFHs and RFHs, as shown in Fig. 13, proves that the displacement of LFHs and RFHs can be equal by arranging the stiffness of LFHs and RFHs according to the stiffness ratio β. And whether the motor and working stage are rigidly connected or flexibly connected, it will not affect the displacement of flexure hinges.

According to the Eq. (2), the stiffness of IFH, L-LSFH and R-LSFH can be shown in Eq. (12):

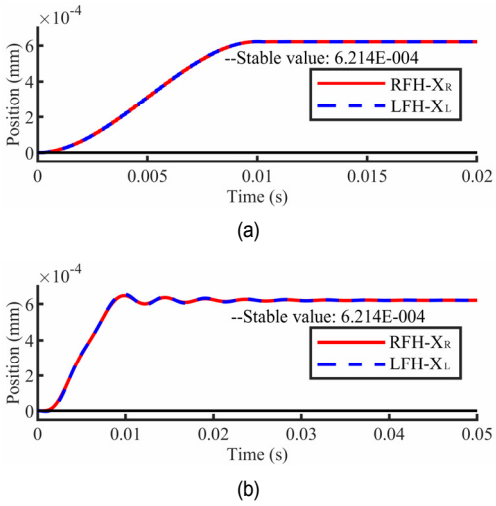

Fig. 13. Flexure hinges displacement curve: (a) rigid connection; (b) flexible connection.

$$K_i = \frac{E_i w_i t_i^3}{l_i^3}, (i = 0,1,2) \quad (12)$$

where the subscript "0" denotes the parameter of IFHs, subscript "1" and "2" denotes the parameter of L-LSFHs and R-LSFHs, respectively. E_0 = 72000 MPa, and $E_1 = E_2$ = 211000 MPa. w_0 = 15 mm, and $w_1 = w_2$ = 28 mm. l_0 = 9 mm, and $l_1 = l_2$ = 3 mm.

Hence, "no deflection constraint" is that the thickness of the three groups of flexure hinges satisfies Eq. (13):

$$\frac{n_0 K_0 + n_1 K_1}{n_0 K_0 + n_2 K_2} = \frac{K_L}{K_R} = \beta \quad (13)$$

where the number of both L-IFHs and R-IFHs are n_0. n_1 and n_2 are the number of L-LSFHs and R-LSFHs, respectively. In this case, n_0 = 8, n_1 = 4, n_2 = 4.

3.2.2 Deformation uniformity constraint

The deformation deviation of different positions of the working stage should be limited to a certain range.

In general, the smaller the stiffness of the flexure hinges, the more uniform the deformation on X-axis, but it is unfavorable from the perspective of safety. The greater the stiffness of the stage, the greater the non-uniformity of the X-axis. Therefore, it is necessary to limit the non-uniformity of the working stage to restrict the maximum stiffness K_{max}. In addition, the total stiffness should not be greater than K_{max} when increasing LSFHs. The determination steps of non-uniformity and K_{max} are as follows.

When there is only IFHs, the thickness relationship of L-IFHs and R-IFHs can be obtained from Eq. (14):

$$n_0 \frac{E_0 w_0 t_L^3}{l_0^3} / n_0 \frac{E_0 w_0 t_R^3}{l_0^3} = \beta \quad (14)$$

Table 2. Deformation non-uniformity of RFSC when different thickness groups are taken for IFHs.

Group	t_R	t_L	N_{X-axis}
1	0.50	0.42	0.43 %
2	0.60	0.51	0.69 %
3	0.70	0.59	1.09 %
4	0.80	0.68	1.54 %
5	0.85	0.72	1.83 %
6	0.90	0.76	2.15 %
7	0.95	0.81	2.43 %
8	1.00	0.85	2.81 %
9	1.05	0.89	3.21 %
10	1.10	0.93	3.64 %
11	1.15	0.97	4.00 %
12	1.20	1.12	4.48 %
13	1.25	1.06	4.98 %
14	1.30	1.10	5.51 %

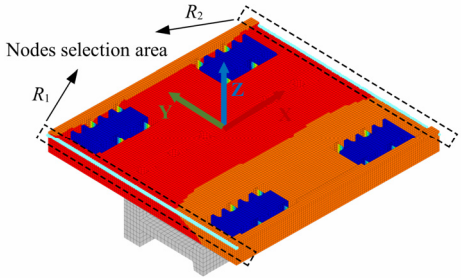

Fig. 14. Select nodes.

where β is determined by Eq. (11), and t_L is the thickness of L-IFHs, and t_R is the thickness of R-IFHs.

Hence, the ratio of thickness is defined as follows:

$$\lambda = \frac{t_u}{t_d} = \sqrt[3]{\beta} \,. \tag{15}$$

Calculate that λ equals 0.8477. The RFCS with only IFHs is driven by 166 N and is statically simulated in HyperWorks, and 14 groups are classified by the thickness selection area of 0.5 mm - 2 mm, as shown in Table 2.

The non-uniformity of the X-axis: take 190 nodes on the two edges of the X-axis, R_1 area and R_2 area respectively, as shown in Fig. 14. Output the node displacement of 190 nodes, calculate the average value, and then find the node displacement with the largest distance from the average value, which is called the maximum deviation value (MDV). Finally, the relative deviation between the MDV and the average value is calculated as the non-uniformity of the X-axis. It is defined as

$$N_{X-axis} = \frac{|Z_{MDC} - Z_{AV}|}{Z_{AV}} \times 100\% \tag{16}$$

where Z_{MDV} is maximum deviation value, and Z_{AV} is average value of nodes displacement.

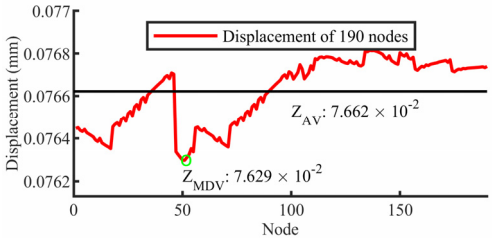

Fig. 15. Nodes displacement curve (X-axis).

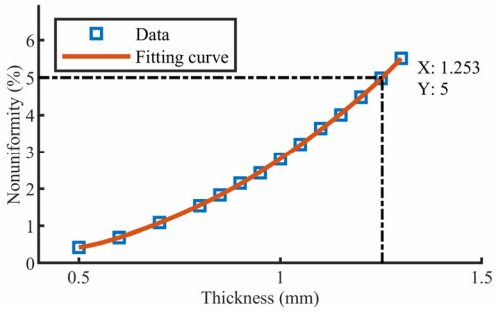

Fig. 16. Fitting curve of N_{X-axis}.

As shown in Fig. 15, it is the nodes displacement curve of the first group of thickness, in which the Z_{AV} is 7.662×10^{-2}, Z_{MDV} is 7.629×10^{-2}, and the calculated the N_{X-axis} of this group is 0.43 %. The results of other groups are shown in Table 2.

The maximum stiffness K_{max}: in order to ensure the high-precision, the N_{X-axis} is less than 5 %. Curve fitting is performed on Table 2 to find the thickness of t_R and t_L corresponding to the maximum stiffness K_{max}. The fitting curve is shown in Fig. 16. When t_R = 1.253 mm and $t_L = t_R\lambda$ = 1.062 mm, the N_{X-axis} is 5 %. The expression of K_{max} is shown in Eq. (17):

$$K_{max} = n_0 \frac{E_0 w_0 t_R^3}{l_0^3} + n_0 \frac{E_0 w_0 t_L^3}{l_0^3} \,. \tag{17}$$

The total stiffness should be less than the maximum stiffness K_{max} when adding LSFHs. Therefore, "deformation uniformity constraint" satisfies the following equation:

$$2n_0K_0 + n_1K_1 + n_2K_2 \le K_{max} \,. \tag{18}$$

3.2.3 Load distribution constraint

LSFHs are the main load-bearing component of the stage, so it is necessary to design the total stiffness of IFHs to be less than that of LSFHs:

$$2n_0K_0 < n_1K_1 + n_2K_2 \,. \tag{19}$$

3.3 Objective function

In order to obtain a high payload capability of RFCS, the stiffness of flexure hinges should be large. Therefore, when the

constraints are satisfied, the three parameters t_0, t_1, and t_2 should take the maximum value. The objective function can be described as

$$Z_{min} = -(t_0 + t_1 + t_2) . \tag{20}$$

3.4 Establishment of optimal design mathematical model

The optimization problem for this design can be described in the following mathematical statement:

Find (t_0, t_1, t_2)

to minimize Z_{min}

subject to

$$\begin{cases} \dfrac{n_0K_0 + n_1K_1}{n_0K_0 + n_2K_2} = \beta \\ 2n_0K_0 + n_1K_1 + n_2K_2 \le K_{\max} \\ 2n_0K_0 < n_1K_1 + n_2K_2 \\ 0.5 \le t_0 \le 2 \\ 0.05 \le t_1 \le 0.35 \\ 0.05 \le t_2 \le 0.35 \end{cases} . \tag{21}$$

According to the above analysis, the nonlinear interior-point optimization technique in MATLAB has been utilized to obtain the structural parameters of the flexure hinges with high deformation uniformity. The results are

$$\begin{cases} t_0 = 0.9249 \\ t_1 = 0.1766 \\ t_2 = 0.2515 \end{cases} . \tag{22}$$

3.5 Simulation verification

In order to verify the effectiveness of the optimal solution, the thickness of the flexure hinges is set as Eq. (22). An FEA is performed with a continuous force of 166N to verify the uniformity in the motion direction and the deformation in the non-motion directions. The deformation uniformity defined in Eq. (16) and the deformations in the non-motion directions are tested for performance estimation. The level of deformation in the non-motion direction is described by the magnitude of the rotation angle on the corresponding coordinate axes, which are defined as:

$$\tan\theta = \frac{|\bar{R}_{1i}| + |\bar{R}_{2i}|}{W}, (i = Y, Z) \tag{23}$$

where $\bar{R}_{1i}$ (i = Y, Z) are the average value of nodes displacement of Y-axis and Z-axis in R_1 area respectively. $\bar{R}_{2i}$ (i = Y, Z) are the average value of nodes displacement of Y-axis and Z-axis in R_2 area respectively. W = 195 mm, it represents the length of the working stage on X-axis.

As a comparison, the RFCS with only IFHs is also tested.

Table 3. The values of $\bar{R}_{1i}$ (i = Y, Z) and $\bar{R}_{2i}$ (i = Y, Z).

Area / Phase	Y-axis		Z-axis	
	$\bar{R}_{1Y}$ (mm)	$\bar{R}_{2Y}$ (mm)	$\bar{R}_{1Z}$ (mm)	$\bar{R}_{2Z}$ (mm)
Before optimization	-10.98×10^{-4}	9.98×10^{-4}	1.75×10^{-4}	-1.60×10^{-4}
After optimization	-9.33×10^{-4}	8.34×10^{-4}	-0.20×10^{-4}	0.27×10^{-4}

Table 4. Error analysis of RFCS simulation results.

Type	Before optimization	After optimization	Error
N_{X-axis}	5.00 %	5.01 %	0.2 %
tan θ value (Y-axis)	1.07E-05	9.06E-06	15.3 %
tan θ value (Z-axis)	1.72E-06	2.40E-07	86 %

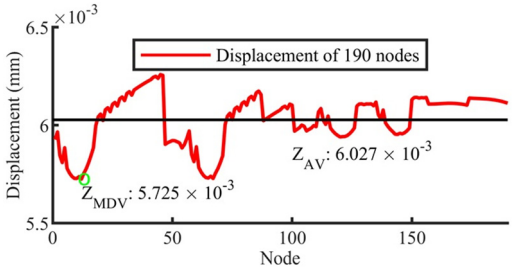

Fig. 17. The nodes displacement curve of after optimization (X-axis).

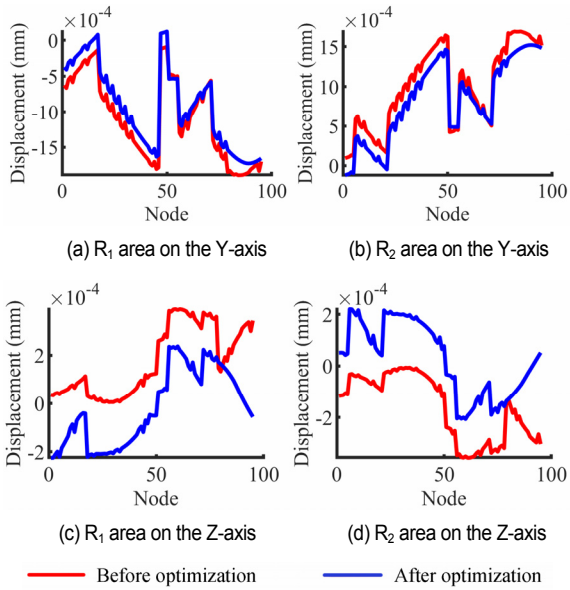

Fig. 18. Nodes displacement curve of working stage on the Y-axis and Z-axis.

The thickness of the IFHs are set as t_R = 1.253 mm and t_L = 1.062 mm, so the total stiffness of the RFCS is equal to the one of the optimal solution. The nodes displacement curve of after optimization on X-axis is shown in Fig. 17. As shown in Fig. 18, it is the nodes displacement of R_1 and R_2 areas of the stage on the Y-axis and Z-axis before and after optimization. The average value of nodes displacement is shown in Table 3. The

result of comparison between the stage with the above optimized result and the stage with only IFHs is shown in Table 4.

As the results show, the error between the $N_{X\text{-}axis}$ after optimization and that before optimization is 0.2 %, which is within a reasonable range. Part of the reason for this error is that the round-off error of thickness values are ignored. In addition, according to the value of tan θ, the deformation on Y-axis and Z-axis is reduced by 15.3 % and 86 %, respectively. The pitching motion of the stage is significantly reduced, which shows the necessity of arranging SFHs.

4. Experiment

4.1 Control system design

According to Fig. 10, the dynamic equation of RFCS is

$$\begin{cases} m_0\ddot{x}_0 = f_0 - k_1(x_0 - x_1) - c_1(\dot{x}_0 - \dot{x}_1) - k_2(x_0 - x_2) - c_2(\dot{x}_0 - \dot{x}_2) \\ \qquad -k_3(x_0 - x_3) - c_3(\dot{x}_0 - \dot{x}_3) - k_4(x_0 - x_4) - c_4(\dot{x}_0 - \dot{x}_4) \\ m_1\ddot{x}_1 = k_1(x_0 - x_1) + c_1(\dot{x}_0 - \dot{x}_1) - f_{\mu 1} \\ m_2\ddot{x}_2 = k_2(x_0 - x_2) + c_2(\dot{x}_0 - \dot{x}_2) - f_{\mu 2} \\ m_3\ddot{x}_3 = k_3(x_0 - x_3) + c_3(\dot{x}_0 - \dot{x}_3) - f_{\mu 3} \\ m_4\ddot{x}_4 = k_4(x_0 - x_4) + c_4(\dot{x}_0 - \dot{x}_4) - f_{\mu 4} \end{cases} \tag{24}$$

A state-space equation can be established based on Eq. (24) as

$$\begin{cases} \dot{\mathbf{X}} = \mathbf{M}\mathbf{X} + \mathbf{F} \\ \mathbf{Y} = \mathbf{C}\mathbf{X} \end{cases} \tag{25}$$

where

$$\begin{cases} \mathbf{M} = \begin{bmatrix} 0 & 0 & 0 & 0 & 0 & 1 & 0 & 0 & 0 & 0 \\ 0 & 0 & 0 & 0 & 0 & 0 & 1 & 0 & 0 & 0 \\ 0 & 0 & 0 & 0 & 0 & 0 & 0 & 1 & 0 & 0 \\ 0 & 0 & 0 & 0 & 0 & 0 & 0 & 0 & 1 & 0 \\ 0 & 0 & 0 & 0 & 0 & 0 & 0 & 0 & 0 & 1 \\ A & \frac{k_1}{m_0} & \frac{k_2}{m_0} & \frac{k_3}{m_0} & \frac{k_4}{m_0} & B & \frac{c_1}{m_0} & \frac{c_2}{m_0} & \frac{c_3}{m_0} & \frac{c_4}{m_0} \\ \frac{k_1}{m_1} & -\frac{k_1}{m_1} & 0 & 0 & 0 & \frac{c_1}{m_1} & -\frac{c_1}{m_1} & 0 & 0 & 0 \\ \frac{k_2}{m_2} & 0 & -\frac{k_2}{m_2} & 0 & 0 & \frac{c_2}{m_2} & 0 & -\frac{c_2}{m_2} & 0 & 0 \\ \frac{k_3}{m_3} & 0 & 0 & -\frac{k_3}{m_3} & 0 & \frac{c_3}{m_3} & 0 & 0 & -\frac{c_3}{m_3} & 0 \\ \frac{k_4}{m_4} & 0 & 0 & 0 & -\frac{k_4}{m_4} & \frac{c_4}{m_4} & 0 & 0 & 0 & -\frac{c_4}{m_4} \end{bmatrix}, \\ A = -(\frac{k_1}{m_0} + \frac{k_2}{m_0} + \frac{k_3}{m_0} + \frac{k_4}{m_0}) \\ B = -(\frac{c_1}{m_0} + \frac{c_2}{m_0} + \frac{c_3}{m_0} + \frac{c_4}{m_0}) \end{cases} \tag{26}$$

$$\mathbf{X} = \begin{bmatrix} x_0 & x_1 & x_2 & x_3 & x_4 & \dot{x}_0 & \dot{x}_1 & \dot{x}_2 & \dot{x}_3 & \dot{x}_4 \end{bmatrix}^T, \tag{27}$$

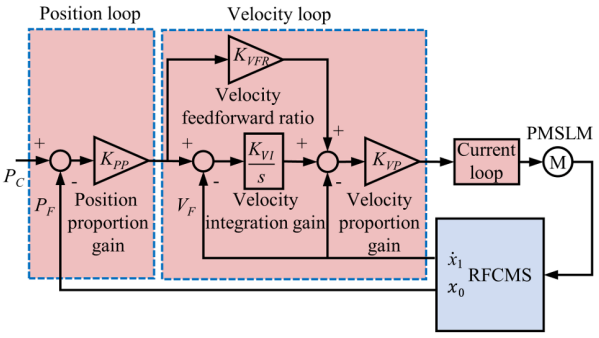

Fig. 19. Control system of RFCMS.

$$\mathbf{F} = \begin{bmatrix} 0 & 0 & 0 & 0 & 0 & \frac{F}{m_0} & 0 & 0 & 0 & 0 \\ 0 & 0 & 0 & 0 & 0 & 0 & -\frac{f_{\mu 1}}{m_1} & 0 & 0 & 0 \\ 0 & 0 & 0 & 0 & 0 & 0 & 0 & -\frac{f_{\mu 2}}{m_2} & 0 & 0 \\ 0 & 0 & 0 & 0 & 0 & 0 & 0 & 0 & -\frac{f_{\mu 3}}{m_3} & 0 \\ 0 & 0 & 0 & 0 & 0 & 0 & 0 & 0 & 0 & -\frac{f_{\mu 4}}{m_4} \end{bmatrix}^T, \tag{28}$$

$$\mathbf{Y} = \begin{bmatrix} y_1 & y_2 \end{bmatrix}^T, \tag{29}$$

$$\mathbf{C} = \begin{bmatrix} 1 & 0 & 0 & 0 & 0 & 0 & 0 & 0 & 0 & 0 \\ 0 & 0 & 0 & 0 & 0 & 0 & 1 & 0 & 0 & 0 \end{bmatrix}. \tag{30}$$

According to the state-space equation, a control system for the RFCMS is built as shown in Fig. 19. A PID controller is used for feedback control of the stage. The displacement of the working stage and the speed of the rigid frames need to be measured for feedback. Because the four rigid frames have high displacement uniformity, only one rigid frame needs to be selected for measurement. Where P_C is the position command; K_{PP} is the position proportion gain, and the value is 0.5; K_{VI} is the velocity integration gain, and the value is 200; K_{VP} is the velocity proportion gain, and the value is 0.1; K_{VFR} is the velocity feedforward ratio, and the value is 0.5; P_F is the position feedback of the working stage, and V_F is the velocity feedback of the frame.

4.2 Construction of experimental set-up

In this section, the design of a prototype for the single-axis RFCMS shown in Fig. 20 is presented (as one possible realization of the proposed concept), which is benchmarked with the PRO190LM (stroke, 500 mm). The stage is guided by a pair of high-rigidity preloaded linear ball mechanical bearings (THK, SHS-15V). A PMSLM (Akribis, AUM4-S4) with 936 N peak and 166 N limited continuous force, powered by a Servotronix controller (Type: CDHD2-0032AAP1), is employed to drive the stage. The stage position is obtained from the linear encoder

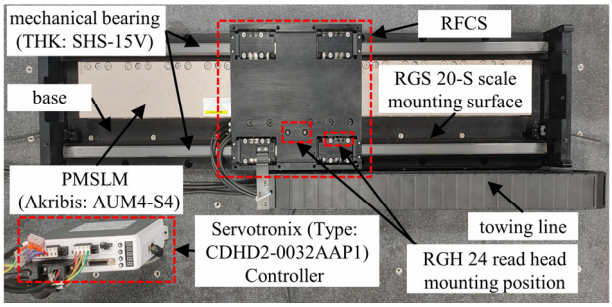

Fig. 20. RFCMS experimental set-up.

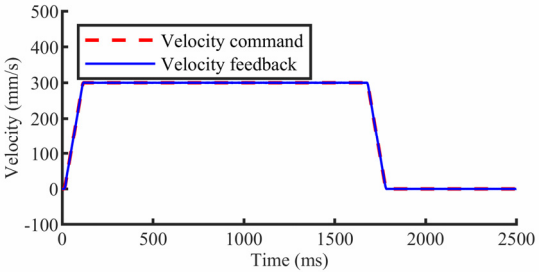

(a)

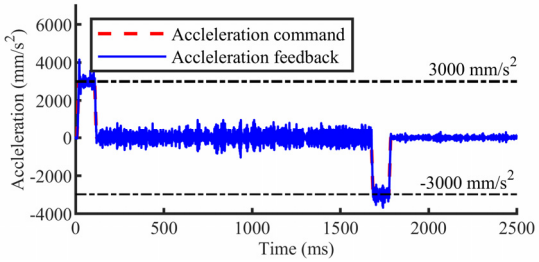

(b)

Fig. 21. Velocity 300 mm/s and acceleration 3000 mm/s^2: (a) velocity curve; (b) acceleration curve.

system (Renishaw, RGH24 read head and RGS20-S scale) with a resolution of 50 nm. The RGS20-S scale is installed on the base of the motion stage, and one RGH24 read head is installed on the working stage and rigid frame, respectively. In order to improve the performance of RFCMS, full-feedback control is applied, where the velocity feedback of rigid frame is used as the velocity loop and position feedback of the working stage is used as the position loop.

The experimental stage is tested for motion of 500 mm stroke at the velocity of 300 mm/s and acceleration of 3000 mm/s^2. The obtained velocity and acceleration curves are shown in Fig. 21. The stage in this paper can meet the requirements of high speed and high acceleration. The position error curve is shown in Fig. 22. Limited by the resolution of the linear encoder system, the steady-state error is 50 nm. In order to verify the accuracy of the optimal method in this paper, as shown in Fig. 23, the laser interferometer is used to detect the BR of the experimental stage (experimental conditions: speed is 300 mm/s, acceleration is 3000 mm/s^2, stroke is 400 mm). Select 8 target points (50 mm, 100 mm, 150 mm, 200 mm,

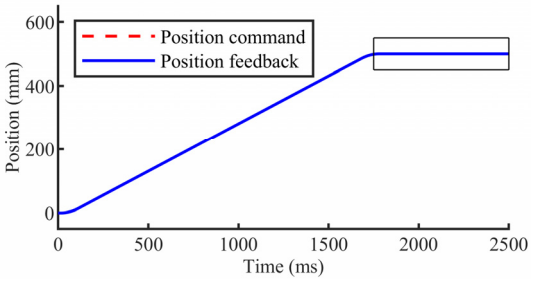

(a)

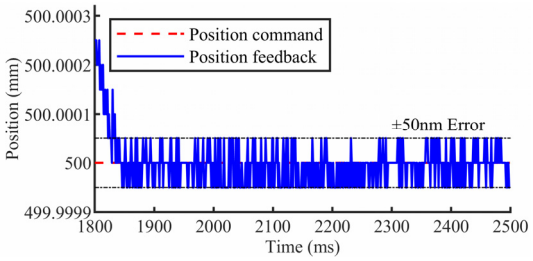

(b)

Fig. 22. Position error curve: (a) the global curve; (b) a local enlargement, and the steady-state error is between ± 50 nm.

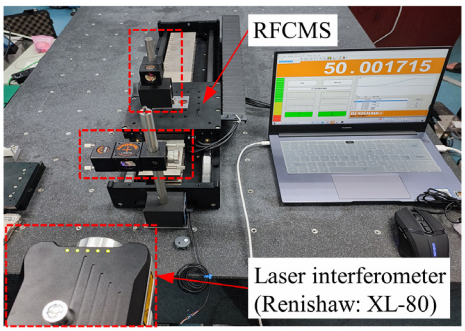

Fig. 23. Testing experiment of laser interferometer.

Name	(+) μm	(-) μm	(Bidir) μm
Repeatability (R)	0.5	0.3	0.5

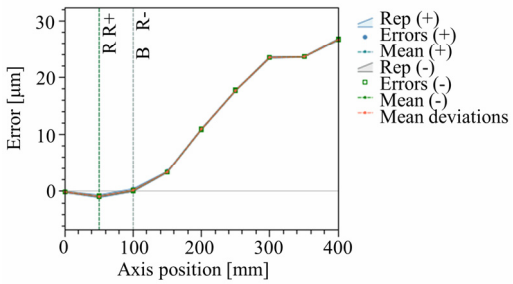

Fig. 24. Bidirectional repeatability test curve.

250 mm, 300 mm, 350 mm, 400 mm) within the 400 mm stroke range of the motion stage, and measure all target points back and forth for 3 cycles. The experiment adopts the standard GB/T17421.2000 to generate the curve and results as shown in Fig. 24. Finally, the BR is measured to be ±0.25 μm.

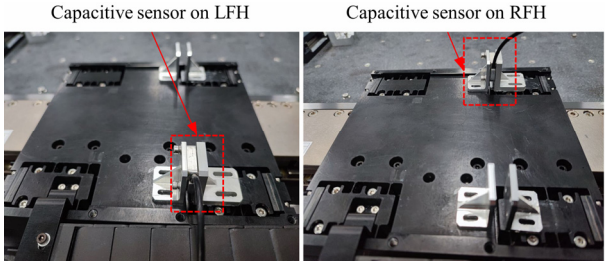

Fig. 25. Installation of capacitive sensor: (a) capacitive sensor on LFH; (b) capacitive sensor on RFH.

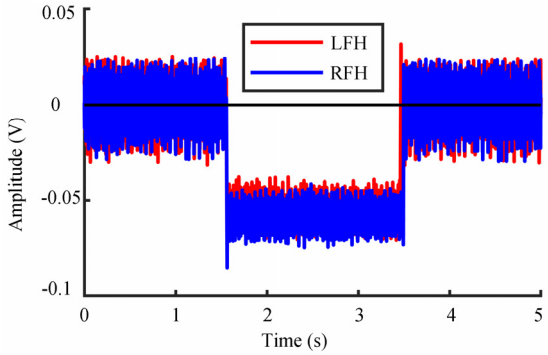

Fig. 26. Deformation amplitude of flexure hinges.

In addition, to further prove the superiority of the proposed method, the maximum static friction is applied to the working stage, and the capacitive sensor (Type: NS-CDCS20L-400) is used to detect the deformation of the flexure hinges in Fig. 25. It is installed between the rigid frame and the working stage. The average deformation amplitude of LFH is -0.054 V and that of RFH is -0.058 V as shown in Fig. 26. The range of the capacitive sensor is 400 μm and the supply voltage is ±10 V. The displacement values converted from the average deformation amplitude are 1.08 μm and 1.16 μm with the error of only ± 3.7 %, which proves the high deformation uniformity of the RFCMS.

5. Conclusions

This paper proposes a long-stroke RFCMS driven by PMSLM eccentricity. This design possesses three advantages: the elastic deformation of flexure hinges are used to produce vibration and compensate the friction dead zone, and the stroke and precision of the motion stage are synchronously improved; an optimization method is proposed, which uses asymmetric flexure hinges to improve the deformation uniformity on the working stage under eccentric force, and reduce the deformation in the non-motion direction; high precision can be achieved with low resolution, which means lower cost. To verify the effectiveness of the proposed design, an RFCMS with 500 mm stroke is developed in this paper. The realized BR is ±0.25 μm while the resolution is only 50 nm. Compared with the PRO190LM with the same stroke, the BR is ±0.4 μm at 5 nm or 10 nm resolution. The precision of RFCMS is improved by 37.5 %. Most importantly, the displacement difference of LFHs and RFHs is only ±3.7 %, which proves the feasibility of the design method of RFCMS driven by PMSLM eccentricity in engineering application. This study considers the deformation uniformity of the stage and provides a new way for friction compensation, which is of great significance to the design and development of the precision positioning motion stage, especially the motion stage driven by eccentricity.

Acknowledgments

The work is supported in part by a grant from National Natural Science Foundation of China (Grant Nos. 51875108, 51905107); in part by the Natural Science Foundation of Guangdong Province under Grant 2019A1515012004.

References

[1] R.-H. M. Schmidt, Ultra-precision engineering in lithographic exposure equipment for the semiconductor industry, *Phil. Trans. R. Soc., A*, 370 (1973) (2012) 3950-3972.

[2] S. Kang, M. G. Lee and Y.-M. Choi, Six degrees-of-freedom direct-driven nanopositioning stage using crab-leg flexures, *IEEE/ASME Trans. Mechatron*, 25 (2) (2020) 513-525.

[3] F. X. Chen et al., A PZT actuated 6-DOF positioning system for space optics alignment, *IEEE/ASME Trans. Mechatron*, 24 (6) (2019) 2827-2838.

[4] K. Inoue, T. Tanikawa and T. Arai, Micro-manipulation system with a two-fingered micro-hand and its potential application in bioscience, *Journal of Biotechnology*, 133 (2) (2008) 219-224.

[5] R. Lin et al., Design of A flexure-based mixed-kinematic XY high-precision positioning platform with large range, *Mechanism and Machine Theory*, 142 (2019) 103609.

[6] M. Torralba et al., Design optimization for the measurement accuracy improvement of a large range nanopositioning stage, *Sensors*, 16 (1) (2016) 84.

[7] Y. Tian et al., Three flexure hinges for compliant mechanism designs based on dimensionless graph analysis, *Precision Engineering*, 34 (1) (2010) 92-100.

[8] S. Iqbal and A. Malik, A review on MEMS based micro displacement amplification mechanisms, *Sensors and Actuators A: Physical*, 300 (2019) 111666.

[9] B. J. Kenton and K. K. Leang, Design and control of a three-axis serial-kinematic high-bandwidth nanopositioner, *IEEE/ASME Trans. Mechatron.*, 17 (2) (2012) 356-369.

[10] M. Torralba et al., Large range nanopositioning stage design: A three-layer and two-stage platform, *Measurement*, 89 (2016) 55-71.

[11] L. Clark et al., Topology optimisation of bridge input structures with maximal amplification for design of flexure mechanisms, *Mechanism and Machine Theory*, 122 (2018) 113-131.

[12] J.-J. Kim et al., A millimeter-range flexure-based nanopositioning stage using a self-guided displacement amplifica-

tion mechanism, *Mechanism and Machine Theory*, 50 (2012) 109-120.
[13] K.-B. Choi, J. J. Lee and S. Hata, A piezo-driven compliant stage with double mechanical amplification mechanisms arranged in parallel, *Sensors and Actuators A: Physical*, 161 (1-2) (2010) 173-181.
[14] S. B. Choi et al., A magnification device for precision mechanisms featuring piezoactuators and flexure hinges: Design and experimental validation, *Mechanism and Machine Theory*, 42 (9) (2007) 1184-1198.
[15] Q. S. Xu, Design and development of a compact flexure-based XY precision positioning system with centimeter range, *IEEE Trans. Ind. Electron.*, 61 (2) (2014) 893-903.
[16] J. K. Shang et al., A novel voice coil motor-driven compliant micropositioning stage based on flexure mechanism, *Review of Scientific Instruments*, 86 (9) (2015) 095001.
[17] Q. S. Xu, Design, testing and precision control of a novel long-stroke flexure micropositioning system, *Mechanism and Machine Theory*, 70 (2013) 209-224.
[18] L. Y. Zhang et al., Implementation and experiment of an active vibration reduction strategy for macro-micro positioning system, *Precision Engineering*, 51 (2018) 319-330.
[19] Y.-T. Liu, T. Higuchi and R.-F. Fung, A novel precision positioning table utilizing impact force of spring-mounted piezoelectric actuator—part II: theoretical analysis, *Precision Engineering*, 27 (1) (2003) 22-31.
[20] L. Y. Zhang et al., A rapid vibration reduction method for macro–micro composite precision positioning stage, *IEEE Trans. Ind. Electron.*, 64 (1) (2017) 401-411.
[21] Q. S. Xu, Design and development of a flexure-based dual-stage nanopositioning system with minimum interference behavior, *IEEE Trans. Automat. Sci. Eng.*, 9 (3) (2012) 554-563.
[22] L. Y. Zhang, J. Gao and H. Tang, Development and modeling of a macro/micro composite positioning system for microelectronics manufacturing, *Key Engineering Materials*, 679 (2016) 135-142.
[23] L. Y. Zhang, J. Gao and X. Chen, A rapid dynamic positioning method for settling time reduction through a macro-micro composite stage with high positioning accuracy, *IEEE Trans. Ind. Electron.*, 65 (6) (2018) 4849-4860.
[24] H. Shinno, H. Yoshioka and H. Sawano, A newly developed long range positioning table system with a sub-nanometer resolution, *CIRP Annals*, 60 (1) (2011) 403-406.
[25] X. Dong, D. Yoon and C. E. Okwudire, A novel approach for mitigating the effects of pre-rolling/pre-sliding friction on the settling time of rolling bearing nanopositioning stages using high frequency vibration, *Precision Engineering*, 47 (2017) 375-388.
[26] Y. Altintas et al., Machine tool feed drives, *CIRP Annals*, 60 (2) (2011) 779-796.
[27] Aerotech, Inc., *PRO190LM Hardware Manual*, Available: https://www.aerotech.com/wp-content/uploads/2021/01/PRO190LM. pdf.
[28] H. Shinno et al., X-Y-θ nano-positioning table system for a mother machine, *CIRP Annals*, 53 (1) (2004) 337-340.
[29] R. Q. Li et al., Analytical solutions for nonlinear deflections of corner-fillet leaf-springs, *Mechanism and Machine Theory*, 157 (2021) 104182.
[30] Y. S. Du, P. C. Dang and T. M. Li, Design and testing of a novel two-axial flexure-based vibration stage, *J. Vib. Eng. Technol.*, 10 (2) (2022) 499-509.
[31] R. Q. Li et al., A compliant guiding mechanism utilizing orthogonally oriented flexures with enhanced stiffness in degrees-of-constraint, *Mechanism and Machine Theory*, 167 (2022) 104555.

Liyun Su is currently pursuing the doctoral program in mechanical engineering of Guangdong University of Technology, Guangzhou, China. Her research interests include design and optimization of ultra-precision motion stage, and semiconductor manufacturing techniques.

Guanxin Huang is currently an Associate Professor with the School of Electromechanical Engineering, Guangdong University of Technology, Guangzhou, China. His research direction is the optimal design of microelectronic manufacturing equipment.

Ruirui Huang is currently pursuing the M.S. degree with the School of Electromechanical Engineering. His research interests include precision motion control, flexure-based compliant mechanisms, and precision manufacturing equipment applications.

Zhijun Yang is currently a Professor with the School of Electromechanical Engineering, Guangdong University of Technology, Guangzhou, China. His research interests include motion control, semiconductor manufacturing equipment, and the compliant mechanism.